The Response of a Multi-Directional Composite Laminate to Through-Thickness Loading

V.L. Tagarielli, G. Minisgallo, A.J. Mcmillan, N. Petrinic

The Response of a Multi-Directional Composite Laminate to Through-Thickness Loading

V.L. Tagarielli, G. Minisgallo, A.J. McMillan, N. Petrinic

PII: S0266-3538(10)00282-4
DOI: 10.1016/j.compscitech.2010.07.013
Reference: CSTE 4767

To appear in: *Composites Science and Technology*

Received Date: 6 May 2010
Revised Date: 12 July 2010
Accepted Date: 17 July 2010

Please cite this article as: Tagarielli, V.L., Minisgallo, G., McMillan, A.J., Petrinic, N., The Response of a Multi-Directional Composite Laminate to Through-Thickness Loading, *Composites Science and Technology* (2010), doi: 10.1016/j.compscitech.2010.07.013

The Response of a Multi-Directional Composite Laminate to Through-Thickness Loading

V.L. Tagarielli [(a) *], G. Minisgallo[(a)], A.J. McMillan[(b)†] and N. Petrinic[(a)]

(a) Department of Engineering Science - Parks Road, OX1 3PJ Oxford, UK
(b) Rolls-Royce plc, PO Box 31 Derby, DE24 8BJ, UK

Abstract

The through-thickness mechanical response of a carbon fibre / epoxy laminated composite of lay-up $[0/45/-45]_{ns}$ is measured at low rates of strain. Uniaxial tension and compression experiments are carried out on dogbone specimens cut from a thick laminate along different directions, and failure mechanisms are observed via optical and electron microscopy. The effect of direct and shear stresses at the ply interfaces on the onset of failure is measured, and a failure envelope is constructed. The compressive response of specimens of different shape is investigated. Composite beams of different volume and aspect ratios are tested to failure in three-point bending and these tests reveal a strong dependence of the apparent out-of-plane tensile strength of the composite on the beam volume; this effect is modelled by Weibull theory.

Keywords: A. carbon fibres, laminate, polymer matrix composites. B. mechanical properties. C. probabilistic methods

Submitted to *Composites Science and Technology,* May 2010

[*] Corresponding author: Tel. +44(0)1865 273110; E-mail: vito.tagarielli@eng.ox.ac.uk
[†] *Royal Society Industry Fellow, Advanced Composites Centre for Innovation and Science, University of Bristol, 83 Woodland Road, Bristol, BS8 1US, UK*

1 INTRODUCTION

During the past few years both the aerospace and defence industry, driven by the necessity of replacing metallic components with composite parts of higher specific stiffness and strength, have driven the development of manufacturing methods to obtain high quality thick laminated composite architectures. While traditionally composite components have been limited to thin shells loaded primarily in-plane, new-generation manufacturing capabilities enable the design of composite components possessing thick sections and subject to significantly tri-axial states of stress.

With the main airframe constructors (such as Boeing and Airbus) competing to design 50% or more of the Boeing 787 and Airbus A350 airframes in composite, a thorough understanding of the through-thickness (TT) response of composite laminates is required.

Experimental measurement of the TT response of composite laminates has traditionally been difficult due to the challenges posed to manufacture sufficiently high quality thick laminated plates. Several authors have conducted combined compression and shear experiments on small off-axis prismatic samples (see for example [1][2]) or on short hollow cylinders subjected to compression and torsion [3][4] but the state of stress induced in such samples is not uniform and the measured response is largely affected by boundary conditions.

Measuring the TT response in combined tension and shear is even more difficult: shear testing is often conducted by short beam bending or notched sample compression tests [5], again characterized by a non-uniform stress distribution across the sample. While some authors have reported results from quasi-static tensile tests conducted on dogbone specimens of short gauge-length [2], the majority of the TT tensile data in the literature was produced by indirect test methods, such as four-point bending of curved beams [6][7][8] and three-point bending of U-shaped [9] and C-shaped beams [10]. All the above test methods are characterised by a non-uniform, tri-axial state of stress which makes interpretation of experimental results difficult; furthermore, these test methods can be employed to evaluate the TT tensile strength of composites but not the associated stress versus strain response.

Existing experimental evidence suggests that the onset of through-thickness failure of composite laminates depends on both direct and shear interlaminar stresses, with a failure envelope of quadratic shape. A number of failure models (e.g. [11],[12],[13],[14],[15]) can successfully predict the onset of TT failure in fibre composites; while these phenomenological models are very effective for brittle matrix materials, they do not offer much insight into the mechanisms of TT failure when more ductile resins are employed.

A number of recently developed composite matrix materials achieve enhanced ductility due to the presence of toughening agents [16]. Polymers of high ductility are known to form shear bands [17][18] and the inhomogeneous microstructure of fibre composites is expected to enhance strain localization in the matrix [19]. In order to understand these plastic mechanisms, several authors (see for example [20],[21]) begin to attempt modelling of the TT response of fibre composites from a micromechanical point of view; detailed observations of the TT failure mechanisms are now needed to validate these micromechanical models.

The complex and irregular microstructure of fibre composites induces a stochastic nature of failure phenomena, resulting in scaling of the measured strength with specimen volume [22]. These size effects have been investigated extensively [23][24] for the case of fibre-dominated failure mechanisms, and experiments show that the strength can reduce by 50% as the specimen volume is increased by five orders of magnitude (for high-quality carbon / epoxy composites).

In the case of matrix-dominated failure mechanisms, fewer authors have investigated size effects: O'Brien and Salpekar [25] studied the scaling of the in-plane transverse tensile strength of unidirectional composites, while Wisnom and co-workers [7][8] approached the problem of composite laminates subject to TT tension and shear. Again, the TT strength was measured indirectly, by using curved beams in bending. These authors found that size effects for matrix-dominated failure modes appear to be more pronounced than those for fibre-dominated failure: a reduction in strength of 50% can be achieved by increasing the specimen volume by three orders of magnitude. This implies that stochastic aspects of the TT strength of composite laminate cannot be

neglected in the design phase, and that more testing and modelling are needed to develop a deeper understanding of these phenomena.

The present study reports results from tension and compression tests performed on large dogbone specimens cut at different angles from a thick composite laminate (thickness greater than 100 mm), together with observations of deformation and failure mechanisms by in-situ optical microscopy or post-mortem electron microscopy. The scatter on the TT tensile strength of the composite laminate is measured and a size effect is detected by conducting three-point bending tests on samples of different volume.

The outline of the paper is as follows: in Section 2 we describe the material under investigation and give details of the experiments performed; in Section 3 we analyse the observed size effect in the context of Weibull's theory [26]; in Section 4 we discuss results from the study.

2 EXPERIMENTAL INVESTIGATION

2.1 Material and specimen preparation

A carbon fibre / epoxy laminated composite was employed in this study. Each lamina consisted of a unidirectional composite with fibre volume fraction $\varphi_{\mathrm{f}} = 0.65$. High tensile strength carbon fibres (HTS-268-1200) of diameter 6 μm were employed, while the resin was a toughened Epoxy (977-2) produced by CYCOM®. Relevant mechanical properties of fibres and resins were obtained from manufacturer data sheets and are listed in Table 1.

Composite plates of lay-up $[0/45/-45]_{ns}$ (with occasional doubled-up laminae) were produced by consolidating a stack of prepregs in an autoclave. The final plate had a thickness of about 100 mm, while each lamina had a thickness of 0.3 mm. Manufacturing defects, in the form of undulations of the laminae in the *x*-*z* plane (*x* coincides with the nominal fibre direction of laminae oriented at 0° while *z* represents the through-thickness direction, see Fig. 1a) were present in some of the composite

plates. The amplitude and wavelength of the undulations were around 3 mm and 100 mm, respectively.

Thin slices of thickness 4 mm parallel to the *y*-*z* plane were water-jet cut from the plates, and flat dogbone specimens of gauge length 12 mm were then water-jet cut from these slices. The specimens were subsequently ground to a cross-section of 5 x 3.5 mm and polished to a surface roughness of approximately 5 μm. We shall refer to the above specimen geometry as S1.

The axis of the S1 dogbone samples, denoted by *Z*, formed an angle α with the *z* axis, chosen to be 0, 15° or 45° (see Fig. 1b). The presence of waviness of the laminae in the *x*-*z* plane resulted in a small angle β between *x* and *X*, varying from sample to sample. This angle was measured in an optical microscope and allowed calculating the direction of the normal unit vector to the plane of the lamina for each specimen, denoted by $\underline{n}$. The fibre direction (denoted by $\underline{l}$) and the transverse direction (denoted by $\underline{m}$) were also calculated for each lamina. The angle formed by $\underline{n}$ and the loading direction *Z* is denoted by θ.

Additional specimens were cut from the composite plates which did not present ply waviness, namely:

- *compression specimens S2*: these were prismatic specimens of square cross-section of dimension 4.2 x 4.2 x 5 mm, with sides parallel to the *x*, *y* and *z* axes, respectively,
- *compression specimens S3*: prismatic specimens of circular cross-section of diameter 4.7 mm and height 12 mm, with axis parallel to the *z* direction, and
- *tension specimens S4*: axisymmetric specimens of dogbone profile, with gauge length of 12 mm and gauge diameter of 3.7 mm, with ply interfaces perpendicular to the loading direction.

All samples were ground and polished to a roughness of 5 μm. Note that specimens S1, S2 and S3 have the same cross-sectional area, and specimens S1 and S3 also possess equal gauge volume.

2.2 Measured compressive and tensile response

Dogbone specimens of geometry S1 and different values of θ were tested in both uniaxial compression and tension at a nominal strain rate of $10^{-3}\,s^{-1}$, and the deformation and failure mechanisms were observed using an optical microscope. The load was applied by a screw-driven test machine and measured by a resistive load cell; the strain in the gauge section was measured by both a non-contact laser extensometer and an axial strain gauge (of grid length 2 mm) adhered to the sample at the centre of the gauge section.

In compression experiments a loading rig, comprising hardened steel clamps and an alignment system, was used to grip the specimen; the loading rig left a free specimen length of approximately 18 mm between the clamps and was loaded by the cross-head of the testing machine via a spherical bearing system in order to avoid spurious lateral forces and bending moments. In tension experiments the dogbone samples were loaded directly by wedge-action grips.

The measured responses in compression and tension are presented in figures 2a and 2b, respectively, for different values of θ. In compression, the true stress versus strain response of the composite comprised a linear elastic response followed by a non-linear response of pronounced strain hardening. Ultimate failure occurred by propagation of an intra-laminar crack at failure strains ranging from 5% (for $\theta = 45^{o}$) to 15% (for $\theta = 0^{o}$). In uniaxial tension, the composite specimens displayed a linear elastic response followed by a small non-linearity and brittle inter-laminar fracture, with tensile ductility below 1.2% for all values of θ.

Figure 3a presents a comparison of the compressive and tensile uniaxial stress versus strain responses for a specimen S1 with $\theta = 45^{o}$; the figure includes a prediction of the elastic stiffness by laminate theory, based on the assumption of a uniaxial stress state in the gauge section and with the elastic properties of fibres and matrix taken from manufacturer data sheets as in Table 1. A pronounced asymmetry is noted, with the compressive strength much exceeding the tensile strength of the material.

In order to explore the effect of inter-laminar direct and shear stresses on the failure of the composite, a failure stress envelope is constructed; the failure stress σ_f is defined according to the following protocol: in tension, σ_f coincides with the ultimate failure stress of the specimens; in compression, σ_f is taken to be the flow stress at a plastic strain of 0.2%. The average inter-laminar direct and shear stresses at failure, σ_i and τ_i, respectively, are calculated from equilibrium considerations as

$$\sigma_i = \sigma_f \cos^2\theta; \quad \tau_i = \sigma_f \sin\theta\cos\theta \tag{1}$$

The failure envelope, consisting of a plot of τ_i versus σ_i for different values of θ, is presented in Fig. 3b. The shape of the envelope appears to be quadratic and the tension/compression asymmetry is evident.

2.3 Observed deformation and failure mechanisms

A video recording device and a high magnification lens were employed to observe the deformation and failure mechanisms of the composites during the tests described above. After the tests, fractured specimens were observed in an environmental scanning electron microscope (ESEM).

Figure 4a presents a series of six photographs acquired during a compression test on a S1 specimen, with $\theta = 0$; each photograph was acquired at different values of true compressive strain, as indicated in the figure. In all S1 specimens, three doubled-up laminae of lay-up [-45_2,0_2,45_2] were present at the centre of the gauge section, as it can be seen in the photographs of Fig. 4a. In frame 1, corresponding to a true strain of about 4%, we note that initially straight machining marks on the surface of the specimens display some waviness, associated with transverse shear deformation in each lamina. Subsequent ESEM observation of the specimen after the test revealed this shear deformation to be permanent.

With increasing axial strain, the magnitude of the shear deformation in the plies increases (frame2). In frame 3, shear deformation begins to localize along narrow bands as indicated. Shear localization planes in each lamina are parallel to the local fibre direction and inclined at 45˚ on the loading direction. In Fig. 4a the intersections of these planes with the *Y-Z* plane are visible; these intersections are oriented at 45˚ on *Z* in

the case of laminae with fibres running along *X*, but they form an angle of 55˚ with *Z* in laminae whose fibre direction is oriented at ±45° on *X* (*x* and *X* coincide for the specimen in Fig. 4a, i.e., $\beta = 0$). We note that the density of shear localization planes is higher in the doubled-up laminae than in the single laminae. As the axial strain increases, some of the localization bands evolve into microscopic intralaminar cracks (frames 4-5) and finally coalesce into larger cracks spanning two or more laminae (frames 5-6). The unstable propagation of one of these large cracks leads to catastrophic failure.

Figure 4b shows a higher magnification ESEM photograph of the same specimen shown in Fig. 4a subsequent to the test; brighter areas represent resin rich zones, while darker areas are associated with high fibre content. Resin rich zones of irregular thickness are observed at the ply interfaces. Deformation bands of thickness on the order of 20μm are visible, inclined at either 45˚ or 55˚ on the loading direction; these bands have not developed into microcracks but voids are occasionally seen therein.

Deformation and failure of specimens with $\theta = 15^{\circ}$ was similar to that of samples with $\theta = 0$, comprising elasto-plastic transverse shear deformation in each lamina, followed by localization and development of microcracks inclined at 45˚ to the loading direction and lying in planes parallel to the fibre direction. In the case of specimens with $\theta = 45^{\circ}$, propagation of both intralaminar and interlaminar cracks occurred at low levels of axial strains, before plastic deformation was visible in the photographs. However, permanent deformation was also present in these samples, as suggested by the measured stress/strain response and confirmed by ESEM observations after the test.

In tension, brittle failure occurred before any plastic deformation was visible. An interlaminar crack propagated at an interface between two plies, occasionally climbing on to the adjacent ply interfaces. This is evident in the ESEM picture in Fig. 5, showing the fracture surface of a specimen with $\theta = 45^{\circ}$. It is not possible to conclude, from the ESEM observations, at which interface fracture had initiated. Observations of fracture surfaces revealed that fracture was equally likely to be initiated at any interface, independent of the fibre orientation of the laminae sharing the interface.

2.4 Compressive response of specimens of different geometry

The effect of the geometry of the specimen on the compressive response of the composite was explored experimentally. Specimens of geometry S1, S2 and S3 were tested at a strain rate of $10^{-3}\,\mathrm{s}^{-1}$. The prismatic samples S2 and S3 were compressed between two flat platens lubricated by a PTFE spray. In all specimens the normal vector to each lamina was parallel to the loading direction $(\theta = 0)$; the tests were repeated 5 times for each specimen geometry.

Representative stress/strain responses for the three specimen geometries are presented in Fig. 6. All specimens display an initial elastic response followed by a non-linear phase; however, the strain hardening rate is much more pronounced for specimens S2 and S3 than for specimens S1, and ultimate failure of specimens S2 and S3 occurs at higher stresses and smaller strains than for specimens S1. In-situ optical and post-mortem ESEM observations revealed that permanent deformation was present in all samples. The compressive deformation mechanism of specimens S2 and S3 was similar to that described above for specimens S1 but the extent of transverse plastic shearing of the laminae was much less than that observed for specimens S1. Some barrelling was observed for specimens S2 and S3.

2.5 Scatter in the measured tensile strength

As detailed above, the response of the composite in tension was brittle and the measured tensile strength was associated to large data scatter. In order to quantify the variability of this material property, 20 repeated quasi-static tensile tests were conducted on dogbone samples of geometry S4 (all with $\theta = 0$). Wedge action grips were employed to load the specimens at a nominal strain rate of $10^{-3}\,\mathrm{s}^{-1}$.

These measurements are reported in Fig. 7 as a plot of the probability of survivability P_s of the sample as a function of the measured tensile failure stress. The tensile strength ranged from 50 to 85 MPa and the data followed a Weibull [26] distribution

$$P_s = \exp\left(-\left(\sigma_f / \sigma_0\right)^m\right) \tag{2}$$

where σ_0 and m are material properties. A best fit of equation (2) through the data (included in Fig. 7) gave $\sigma_0 = 75\,\mathrm{MPa}$ and $m = 13$ for the reference stress and the

Weibull modulus, respectively. Note that the measured value for m is comparable to that typically reported for low-performance ceramic materials. This value is much smaller than that found by other authors (see for example [24]) for the strength of carbon composites loaded in the fibre direction, typically around $m = 30$.

2.6 Three-point bending experiments

The large scatter in the measured tensile strength of the laminated composite under investigation suggests that measured strength may depend on the specimen size. In order to investigate this, three-point bending experiments were conducted on prismatic beams of different volume.

A sketch of the three-point bending experiment is presented in Fig. 8. The beams had a fixed span $L = 25$ mm; the height h was either 3 or 6 mm, and the width b was 3, 53 or 92 mm. Support and loading was by steel rollers of diameter 12 mm, and the beams were positioned as indicated in Fig. 8, to give deflection in the x - z plane and a bending moment parallel to y (see Fig. 1). Extreme care was taken to align the supporting rig and the loading system, in order to ensure that the loading roller was parallel to the beams surface and that it made contact with these simultaneously at all points along the width b.

The measured load/deflection response up to failure is presented in Fig. 9a as a graph of the normalised transverse load P/b versus mid-span deflection. Two sets of curves are presented for two values of h. The figure includes beam theory predictions of the elastic response of the structure, obtained taking into account deflections due to shear and with the relevant shear moduli calculated with rule of mixtures, based on the fibre volume fraction and the material properties obtained from manufacturer's data-sheets. The measured beam response was elastic to failure and followed the predictions.

We observe that for a given beam height h the maximum tensile stress in the beams scales with P/b. Figure 9a then shows that for each value of h, beams of larger volume (i.e., larger b) fail at lower values of the maximum tensile stress. In order to confirm that this effect is inherent to the composite material rather than an artefact associated with test method or sample geometry, aluminium beams of identical geometry to that of the

composite beams ($h = 3\,\text{mm}$, $b = 3, 53, 92\,\text{mm}$) were tested according to the same protocol.

The bending response of the aluminium beams are presented in Fig. 9b together with a prediction of the elastic response of the structure; the normalised load versus deflection curves are independent of specimen volume. Note that since aluminium has a Young's modulus $E \approx 70$ GPa , while the out-of-plane stiffness of the composite is of the order of 7 GPa, the response of aluminium beams is more sensitive to rig misalignment than that of the composite beams.

The maximum stress at failure in the beams was calculated from the failure load P_f as $\sigma_f = 3P_f L / 2bh^2$; however, in selected experiments, an axial strain gauge was adhered at mid-span to the bottom surface of the beam in the z direction, and the strain reading confirmed the calculated value. A summary of the results of three-point bending tests is presented in Fig. 10. In this figure σ_f is plotted as a function of the beam volume. It is clear that the material strength (ranging from 50 to 150 MPa) is strongly dependent on the specimen volume.

3 ANALYTICAL PREDICTIONS OF THE OBSERVED SIZE EFFECT

Simple analytical models based on Weibull's probability of survivability [26] were constructed in order to aid interpretation of the experimental results in Fig. 10. If the probability of survivability P_s of the material follows the Weibull's distribution given by (2), the corresponding P_s for specimens of different volume V subjected to uniform stress is given by

$$P_s = \exp\left(-\left(V / V_0\right)\left(\sigma_f / \sigma_0\right)^m\right) \tag{3}$$

where V_0 is a reference volume. If the stress is non-uniform across the sample, P_s is

$$P_s = \exp\left(-\frac{1}{V_0}\int_V \left(\frac{\sigma}{\sigma_0}\right)^m dV\right) \tag{4}$$

The physical justification for the integration of $(\sigma/\sigma_0)^m$ over the specimen volume performed in eq. (4) is that the probability of failure of a material point is uniform across the entire volume of the sample and not, for example, higher at the external surface; this assumption appears reasonable for the finely polished specimens tested here.

For a beam in three-point bending the integral in eq. (4) can be solved by assuming the stress distribution predicted by beam theory, and integrating $(\sigma/\sigma_0)^m$ over the lower half of the beam, subjected to tensile stresses (the underlying assumption is that the stress field in the upper part of the beam, subject to compressive stresses, does not contribute to the probability of failure of the sample). This gives

$$\frac{\sigma_f}{\sigma_0} = \left[-2\ln(P_s)(m+1)^2\right]^{\frac{1}{m}} \left(\frac{V}{V_0}\right)^{-1/m}, \tag{5}$$

i.e., the apparent strength of the material scales with the beam volume according to a power-law of exponent -1/*m*, independent of the aspect ratios *b/L* and *h/L*.

Figure 10 includes the strength predictions of eq. (5), with the choices $\sigma_0 = 75\,\text{MPa}$, $m = 13$ and $V_0 = 130\,\text{mm}^3$ (equal to the gauge volume of specimens S4): the band in the figure is bounded by the predictions of eq. (5), with the lower bound corresponding to $P_s = 0.99$ and the upper bound to $P_s = 0.01$. It is clear that eq. (5) captures the dependence of the apparent strength σ_f on the beam volume *V*; on the other hand, not all the data points fall within the predicted failure band: this is justified by the presence of additional sources of data scatter associated with the experiments. For example, it was noted that some of the beams tested presented a slight misalignment of laminae, such that the direction of the applied load formed a small angle with the planes containing the laminae; for these defective beams is therefore (locally) $\theta > 0$ and a stronger tensile response is expected, compared with the case $\theta = 0$ (see Fig. 2b).

The ratio (σ/σ_0) in eq. (2) can be interpreted as a material failure exposure parameter. In the three-point bending experiments conducted here, the composite is subject to shear stresses as well as direct tensile and compressive stresses, and the measurements shown

in the right-hand quadrant of Fig. 3b suggest that a quadratic failure exposure in $\tau_i - \sigma_i$, such as $(\tau_i/\tau_0)^2 + (\sigma_i/\sigma_0)^2$, would be appropriate for the material under investigation. The probability of survivability P_s would then be given by

$$P_s = \exp\left(-\frac{1}{V_0} \int_V \left(\left(\frac{\tau_i}{\tau_0} \right)^2 + \left(\frac{\sigma_i}{\sigma_0} \right)^2 \right)^{m'} dV \right) \tag{6}$$

with $m' = m/2$ so that (6) reduces to (4) if shear stresses are not present. Solution of eq. (6) reveals that the apparent strength of the material scales with the beam volume according to a power-law of exponent $-1/m$, independent of the beams aspect ratios *b/L* and *h/L*

$$\frac{\sigma_f}{\sigma_0} = f\left(m, P_s, \frac{\sigma_0}{\tau_0} \right) \left(\frac{V}{V_0} \right)^{-1/m} \tag{7}$$

Note that τ_i/σ_i increases with increasing *h/L*; using eq. (5) instead of eq. (7) leads to overestimating the beam strength for high values of *h/L*. Equation (7) provides more accurate predictions for the strength of the beams with the higher values of *h*.

4 DISCUSSION OF RESULTS

Compressive response

Measurements and observations reported in this study show that plastic deformation of the epoxy resin occurs when the composite under investigation is loaded by through-thickness compressive stresses much higher than the transverse shear stresses applied. Transverse plastic shear deformation, initially uniform in each lamina, tends to localise within narrow shear bands with increasing axial strain. Then, these shear bands evolve into *intralaminar* microcracks which trigger catastrophic failure. As the applied interlaminar shear stress becomes comparable with the compressive stress $(\theta = 45^o)$, brittle mechanisms lead to failure after some plastic deformation.

Figure 4a shows that the majority of shear bands and microcracks are originated in the thicker doubled-up laminae, independent of their orientation (the three doubled-up laminae in Fig. 4a are oriented at 0, 45 and -45 degrees). This suggests that failure

might be delayed by minimising the lamina thickness, for composites with a ductile matrix.

Comparison of the compressive responses of specimens of different geometry presented in Fig. 6 suggests that the measured through-thickness response is strongly sensitive to boundary conditions: for short prismatic samples the constraint imposed by the contact with the loading platens hampers the occurrence of transverse plastic shearing of the laminae, and the resulting measured response is more brittle than that of dogbone samples.

Specimen geometry must be taken into consideration when interpreting data such as those presented in Fig. 3b. The failure envelope in Fig. 3b was constructed by defining the failure stress in compression as the flow stress at a plastic strain of 0.2%, but a different envelope could be created by defining the compressive failure stress as, for example, the stress at ultimate failure; in both cases, a number of phenomenological failure criteria provides a good fit to the data [2] (Puck's criterion [12] was successfully tried in this study, but this exercise is omitted here for the sake of brevity).

The material response to a macroscopically uniaxial applied compressive stress is that measured on the S1 dogbone specimens, whereas the responses of specimens S2 and S3 are influenced by the applied boundary conditions: friction between specimens and loading platens induces at the ends of specimens S2 and S3 a tri-axial state of stress, the effect of which is more pronounced for specimen S2, of shorter height. Micromechanical models need to be constructed to predict the elasto-plastic response of laminated composites loaded in combined through-thickness compression and shear.

Tensile response

In combined out-of-plane tension and shear, the composite material failure always occurs at ply interfaces, after negligible plastic deformation, by unstable propagation of *interlaminar* cracks. The corresponding stress/strain response is approximately linear to failure, and the ultimate failure stress is characterised by large scatter. The level of scatter on the failure stress is much higher in tension than in compression: 35% and 13%, respectively, for $\theta = 0$. Bending tests confirm that the strength of the material is strongly dependent on the volume of the test specimen (Fig. 10).

The observations above support the notion that the out-of-plane tensile failure of laminated composites is a phenomenon of pronounced stochastic nature, and this must be taken into account in the design of thick composite components. Weibull's theory was employed successfully in this study to predict the size effect observed in the three-point bending experiments. Additional work needs to be performed in order to account for the stochastic nature of the through-thickness strength of laminated composites in numerical simulations. The dependence of the through-thickness strength of composites upon the volume of material under stress should be incorporated in numerical models for dynamic failure: rapid propagation of elastic wave-fronts in composites results in a probability of failure which varies as a function of time.

5 CONCLUDING REMARKS

This study has focussed on the response of multidirectional laminated carbon/epoxy composites loaded through-thickness by direct and shear stresses. Stress versus strain responses have been measured and deformation and failure mechanisms have been observed. The main conclusions are:

- In presence of high through-thickness compressive stresses (compared to interlaminar shear stresses), deformation involves plastic deformation of the matrix; failure is initiated by localization of deformation within narrow shear bands which evolve into *intralaminar* microcracks at high loads.
- The measured compressive through-thickness response is highly sensitive to specimen geometry.
- The tensile through-thickness response is approximately linear elastic; failure occurs at the ply interfaces by unstable propagation of *interlaminar* cracks.
- Out-of-plane tensile failure is associated with a high degree of scatter, of the same order to that reported for low-performance ceramics; this results in a strong dependence of the apparent material strength upon the specimen volume. This effect can be predicted by Weibull's theory.

ACKNOWLEDGEMENTS

The authors are grateful to GKN and Rolls-Royce for the supply of the composite material. We thank Annegret Siebert at Rolls-Royce for arranging the financial support of a six-month internship of Giordano Minisgallo at the University of Oxford. Alison McMillan acknowledges the support of the Royal Society and the University of Bristol through the Royal Society Industrial Fellowship scheme. Vito Tagarielli thanks Stuart Carter, Neil Warland and Wolfgang Mix for their technical support with experiments and Prof Alan Cocks for helpful conversations.

REFERENCES

[1] Bing Q. and Sun C.T., 2008. *Specimen size effect in off-axis compression tests of fiber* composites, Composites Part B: Engineering, 39(1):20-26.

[2] Daniel I.M., Luo J-J., Schubel P.M. and Werner B.T., 2009. *Interfiber/interlaminar failure of composites under multi-axial states of stress*, Composite Science and Technolgoy, 69(6):764-771.

[3] DeTeresa S.J., Freeman D.C. and Groves S.E., 1998. *Fatigue and Failure of Fiber Composites Under Combined Interlaminar Stresses*, In Proceedings 13th Annual Tech. Conf. Compos. Mater., American Society for Composites, Baltimore, MD.

[4] DeTeresa S.J, Freeman D.C. and Groves S.E., 2004. *The Effects of Through-thickness Compression on the Interlaminar Shear Response of Laminated Fiber Composites*, J. Comp. Mater., 38(8):681–697.

[5] Broughton W.R. and Gower M.R.L., 2001. *Through-Thickness Testing of Polymer Matrix Composites*, material note MATC(MN)06, National Physical Laboratory, Middlesex, UK.

[6] Jackson W.C. and Martin R.H., 1992. *An interlaminar tensile strength specimen*, Compos. Mater., 11:333–354.

[7] Wisnom M.R. and Jones M.I., 1996. *Size effects in interlaminar tensile and shear strength of unidirectional glass fibre/epoxy*, J. Reinf. Plast. Comp., 15:2–15.

[8] Wisnom M.R., Jones M.I. and Hill G.F.J., 2001. *Interlaminar tensile strength of carbon fibre-epoxy – specimen size, layup and manufacturing effects*, Adv. Compos. Lett., 11:171–177.

[9] Wisnom M.R., Petrossian Z.J. and Jones M.I., 1996. *Interlaminar failure of unidirectional glass/epoxy due to combined through thickness shear and tension*, Compos. Part A, 27A: 921–929.

[10] Cui G.Y. and Ruiz C., 1995. *Through thickness failure of laminated C/epoxy composites under combined stresses*, Compos. Sci. Technol., 53: 253–258.

[11] Hashin Z., 1980. *Failure criteria for unidirectional fiber composites*, J. Appl. Mech., 47: 329–334.

[12] Puck A. and Schürmann H., 1998. *Failure analysis of FRP laminates by means of physically based phenomenological models*, Compos. Sci. Technol., 58:1045–1067.

[13] Pinho S.T., Iannucci L. and Robinson P., 2006. *Physically-based failure models and criteria for laminated fibre-reinforced composites with emphasis on fibre-kinking. Part I: devlopment*, Compos. Part A, 37: 63–73.

[14] Davila C.G., Camanho P.P. and Rose C.A., 2005. *Failure criteria for frp* laminates, Journal of Composite Materials, 39:323.

[15] Wiegand J., Petrinic N. and Elliot B., 2008. *An algorithm for determination of the fracture angle for three-dimensional Puck matrix failure criterion for UD composites,* Comp. Sci. and Tech., 68(12):2511-2517.

[16] Yee A.F., Du J. and Thouless M.D., 2000. *Toughening of epoxies*, Polymer Blends, Wiley (2000), pp.225–267.

[17] Chau C.C. and Li J.M.C., 1981. *Fracture of shear bands in atactic polystyrene*, J. Mater. Sci., 16(7):1858-1873.

[18] Liu C., Huang Y. and Stout M.G., 1998. *Enhanced mode-II fracture toughness of an epoxy resin due to shear banding*, Acta Materialia, 46(16):5647-5661.

[19] Zhou M., 1998. *The growth of shear bands in composite microstructures*, Int. J. of Plasticity, 14(8):733-754.

[20] Totry E., Gonzales C. and LLorca J., 2008. *Failure locus of fiber-reinforced composites under transverse compression and out-of-plane shear*, Comp. Sci. and Tech., 68(3-4):829-839.

[21] Totry E., Molina-Aldareguia J.M., Gonzales C. and LLorca J., 2010. *Effect of fiber, matrix and interface properties on the in-plane shear deformation of carbon-fiber reinforced composites*, Comp. Sci. and Tech., in press.

[22] Wisnom M.R., 1999. *Size effects in the testing of fibre-composite materials*, Composites Science and Technology, 59:1937-1957.

[23] Gurvich M.R and Pipes R.B., 1995. *Strength size effect of laminated composites*, Composites Science and Technology, 55:93-105.

[24] Lavoie J.A., Soutis C. and Morton J., 2000. *Apparent strength scaling in continuous fiber composite laminates*, Composites Science and Technology, 60:283-299.

[25] O'Brien T.K. and Salpekar S.A., 1993. *Scale effects on the transverse tensile strength of graphite epoxy composites*, Composite Materials: testing and design, ed. E Camponeschi, Vol 11, ASTM STP 1206, pp23-52.

[26] Weibull W., 1951. *A statistical distribution function of wide applicability*, Journal of Applied Mechanics, 18:293-297.

FIGURE AND TABLE CAPTIONS

Table 1. Mechanical properties of the fibres and resin employed to manufacture the composite under investigation, obtained from manufacturers data sheet.

Fig. 1. (a) Sketch of the laminate lay-up and lay-up coordinate system. (b) Sketch of the orientation of ply interfaces in the gauge portion of test specimens.

Fig. 2. Measured stress/strain responses of specimens of type S1 up to failure; (a) compressive response for different values of θ, and (b) tensile response for different values of θ.

Fig. 3. (a) Comparison of the tensile and compressive responses of specimens with $\theta \approx 45^{o}$; the figure includes a prediction of the elastic response. (b) measured effect of the direct and shear stresses at the ply interfaces on the onset of TT failure of the composite laminate under investigation.

Fig. 4. (a) Observed mechanisms of deformation and fracture for a specimen S1 with $\theta \approx 0$, loaded in compression. Each photograph corresponds to the level of axial strain indicated. (b) ESEM image of a specimen S1 with $\theta \approx 0$ after a compression test. Resin rich ply interfaces are visible, as well as shear bands, of width of approximately 20 μm, oriented at 45° on the loading direction.

Fig. 5. ESEM image of the fracture surface of a specimen S1 with $\theta \approx 45^{o}$ tested in tension, showing evidence of interlaminar fracture.

Fig. 6. Comparison of the compressive stress versus strain response of composite specimens S1, S2 and S3 up to failure ($\theta = 0$).

Fig. 7. Probability of survivability as a function of the applied uniaxial stress for specimens of type S4 ($\theta = 0$) loaded in tension. The figure includes a best fit of a Weibull probability distribution through the data (eq. (2)).

Fig. 8. Sketch of the three-point bending tests performed on composite beams of different volume.

Fig. 9. (a) Measured and predicted normalized load versus mid-span deflection responses up to failure for composite beams of two different thicknesses. The prediction is obtained by beam theory and includes the effect of deflections due to shear. (b) Measured and predicted normalized load versus mid-span deflection responses for

aluminium beams of the geometry indicated. Tests were interrupted at a deflection of 0.5 mm.

Fig. 10. Maximum tensile stress at failure versus specimen volume for the beam bending experiments. The failure stress decreases with increasing beam volume; the figure includes prediction from eqns. (5) and (7).

	density, kg m^{-3}	*elastic modulus*, GPa	*transverse elastic modulus*, GPa	*tensile strength*, MPa	*elongation at failure*	*Poisson's ratio* (ν_{12})
fibres	1740	238	35	4240	1.8%	0.2
matrix	1310	3.52	-	81	-	0.39

Table 1. Mechanical properties of the fibres and resin employed to manufacture the composite under investigation, obtained from manufacturers data sheet.

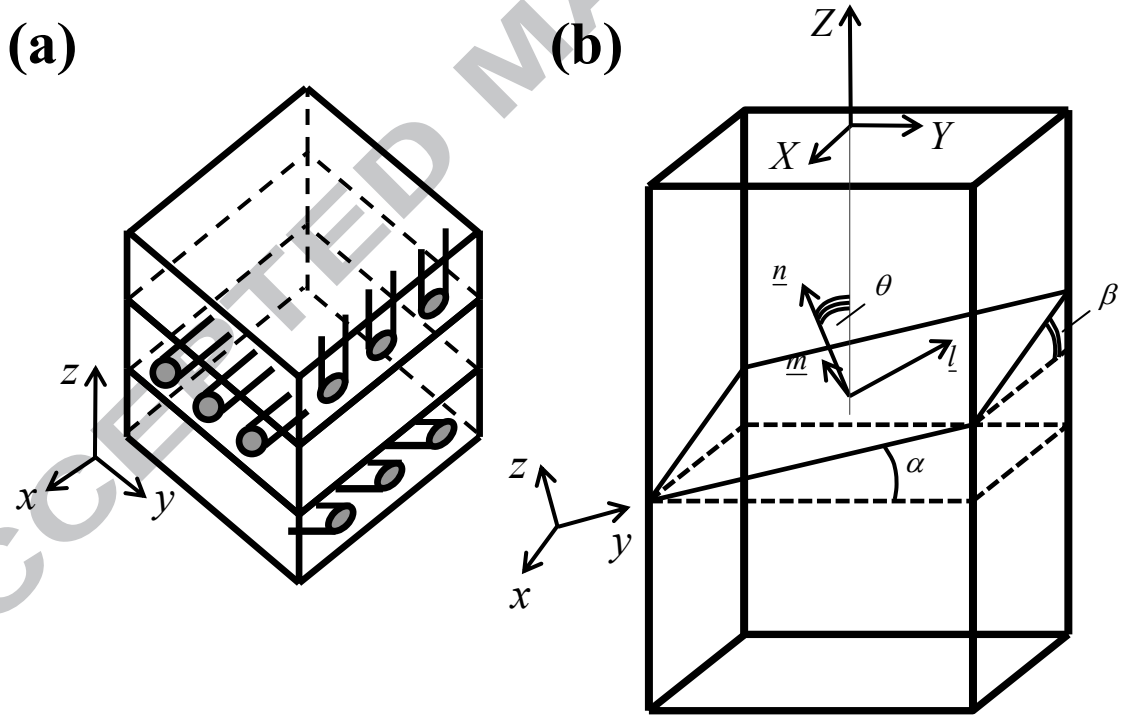

Fig. 1. (a) Sketch of the laminate lay-up and lay-up coordinate system. (b) Sketch of the orientation of ply interfaces in the gauge portion of test specimens.

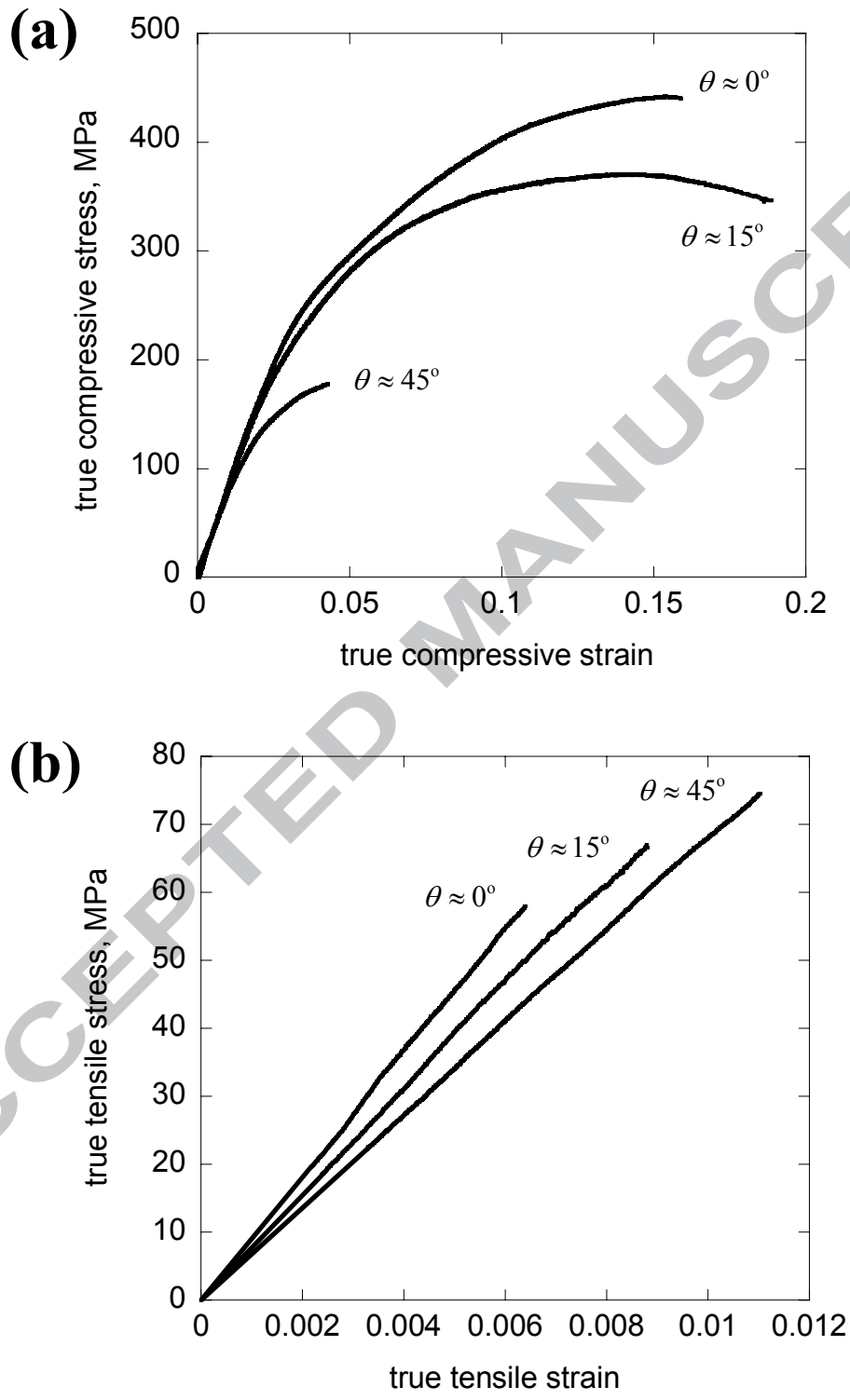

Fig. 2. Measured stress/strain responses of specimens of type S1 up to failure; (a) compressive response for different values of θ, and (b) tensile response for different values of θ.

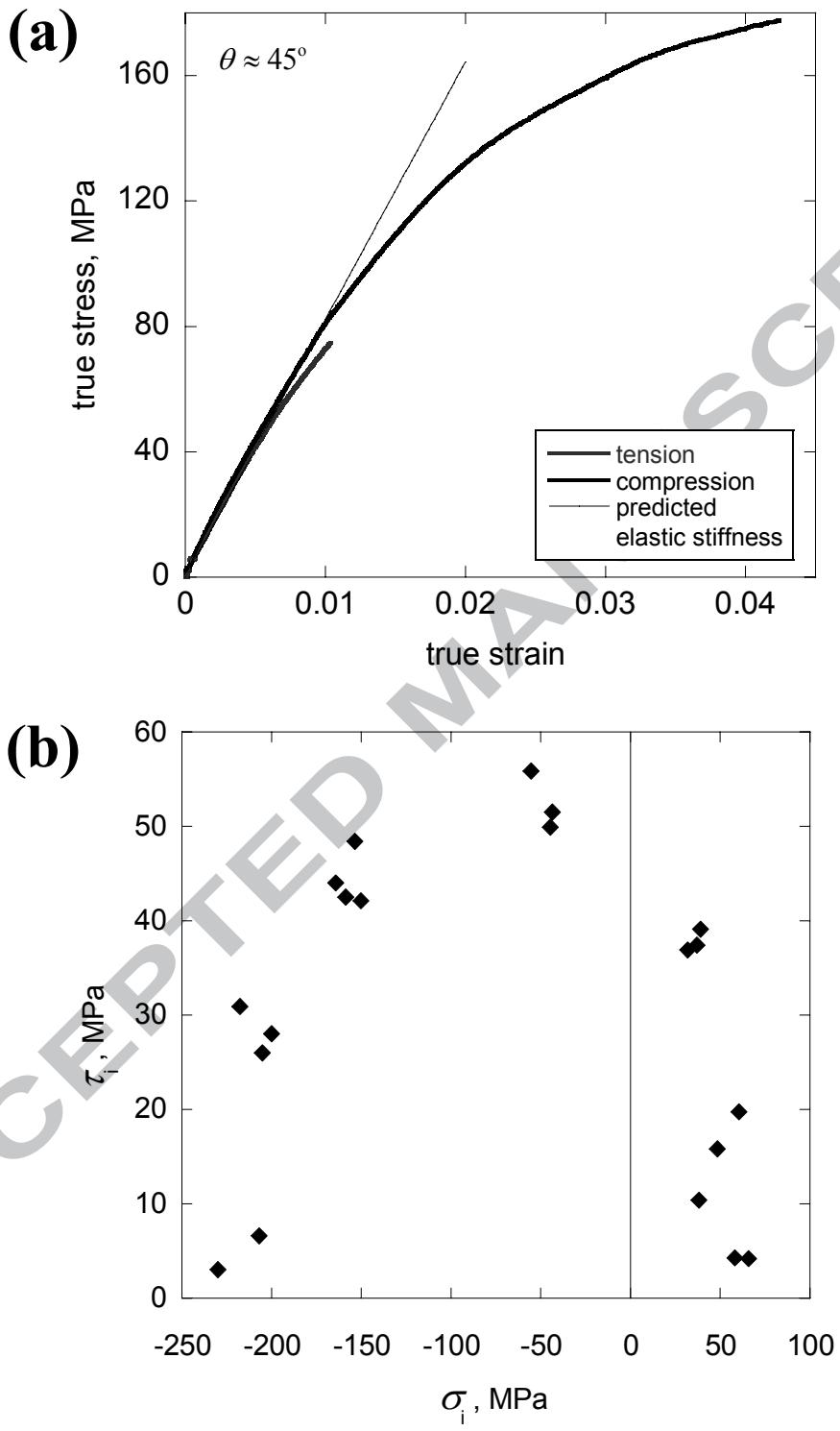

Fig. 3. (a) Comparison of the tensile and compressive responses of specimens with $\theta \approx 45^{o}$; the figure includes a prediction of the elastic response. (b) measured effect of the direct and shear stresses at the ply interfaces on the onset of TT failure of the composite laminate under investigation.

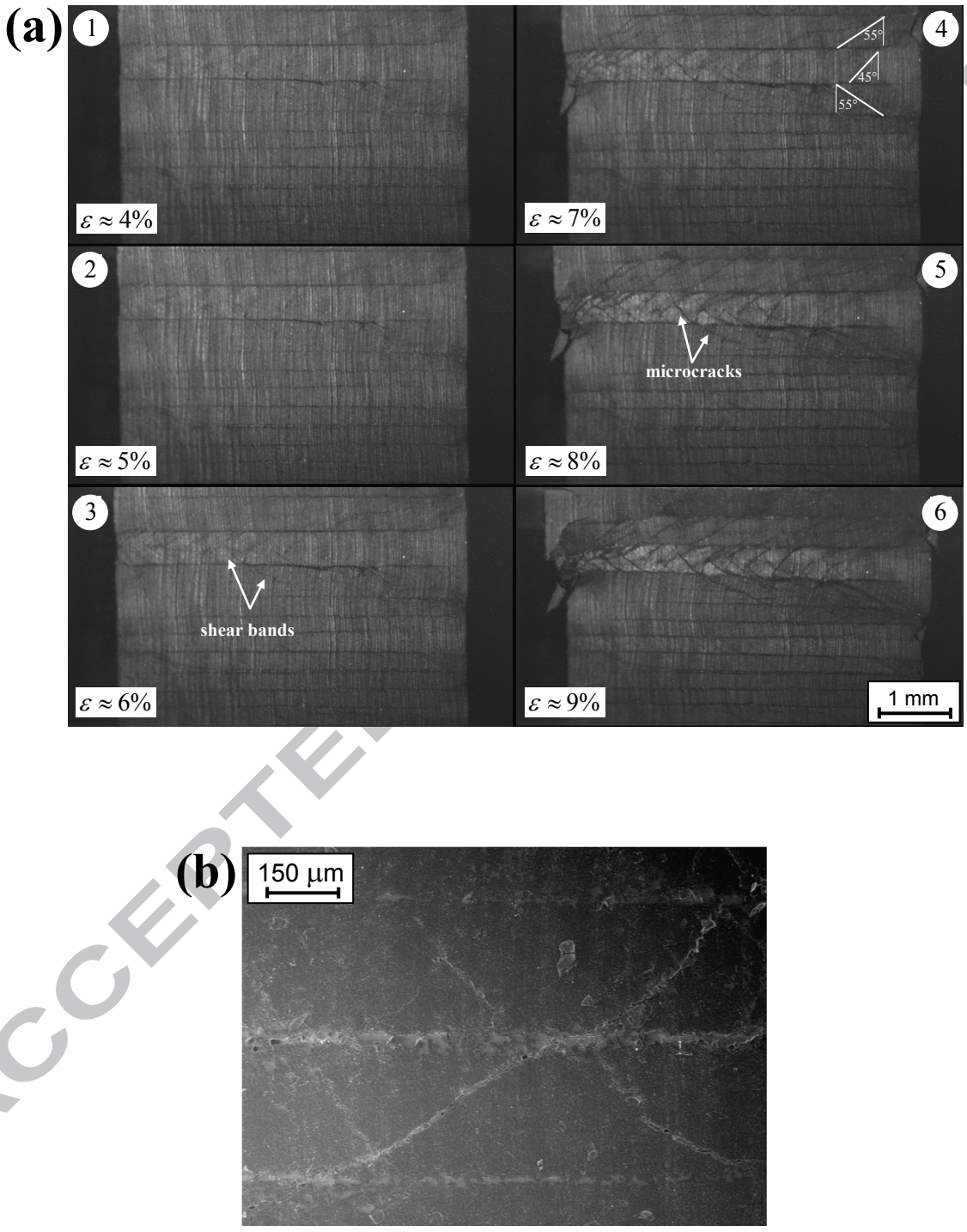

Fig. 4. (a) Observed mechanisms of deformation and fracture for a specimen S1 with $\theta \approx 0$, loaded in compression. Each photograph corresponds to the level of axial strain indicated. (b) ESEM image of a specimen S1 with $\theta \approx 0$ after a compression test. Resin rich ply interfaces are visible, as well as shear bands, of width of approximately 20 μm, oriented at 45° on the loading direction.

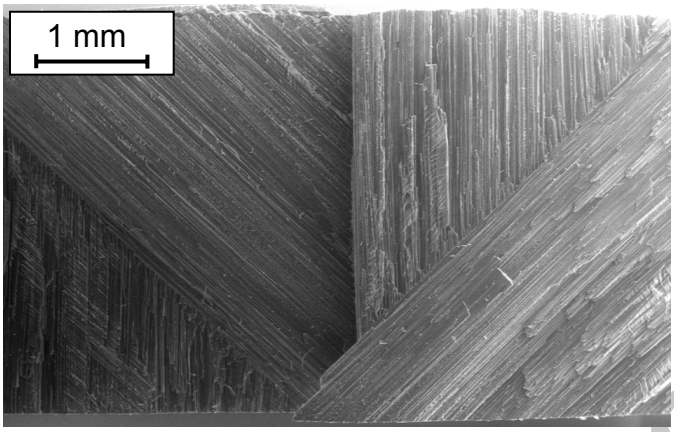

Fig. 5. ESEM image of the fracture surface of a specimen S1 with $\theta \approx 45^{o}$ tested in tension, showing evidence of interlaminar fracture.

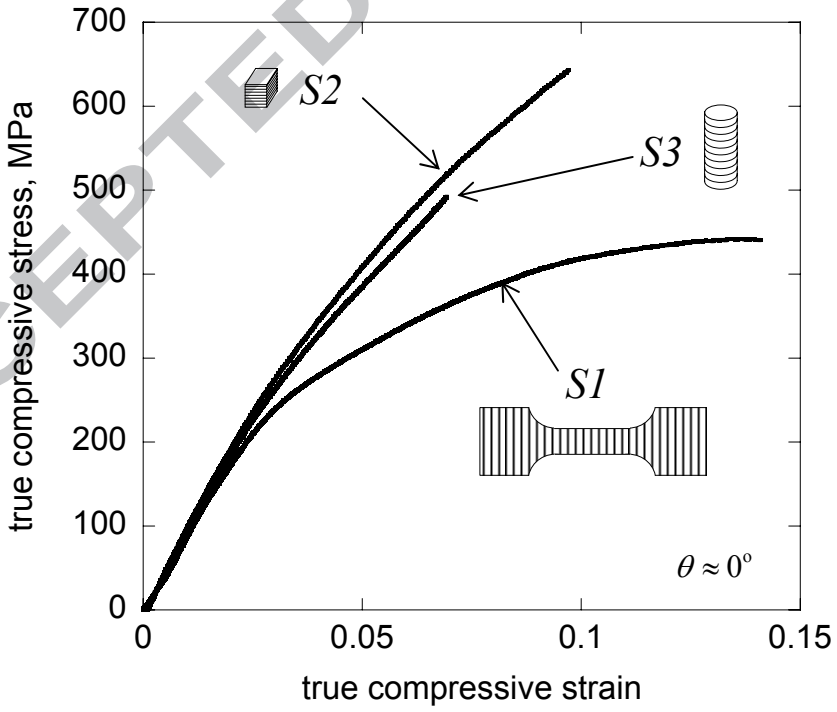

Fig. 6. Comparison of the compressive stress versus strain response of composite specimens S1, S2 and S3 up to failure ($\theta = 0$).

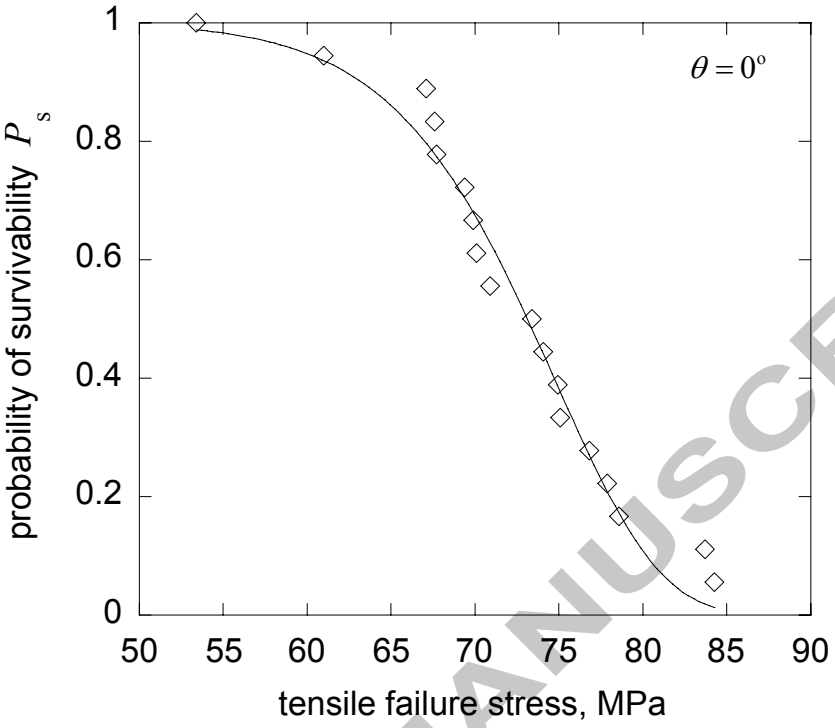

Fig. 7. Probability of survivability as a function of the applied uniaxial stress for specimens of type S4 ($\theta = 0$) loaded in tension. The figure includes a best fit of a Weibull probability distribution through the data (eq. (2)).

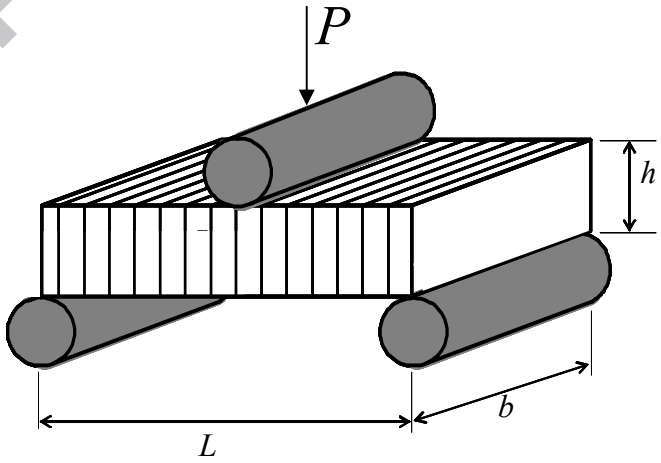

Fig. 8. Sketch of the three-point bending tests performed on composite beams of different volume.

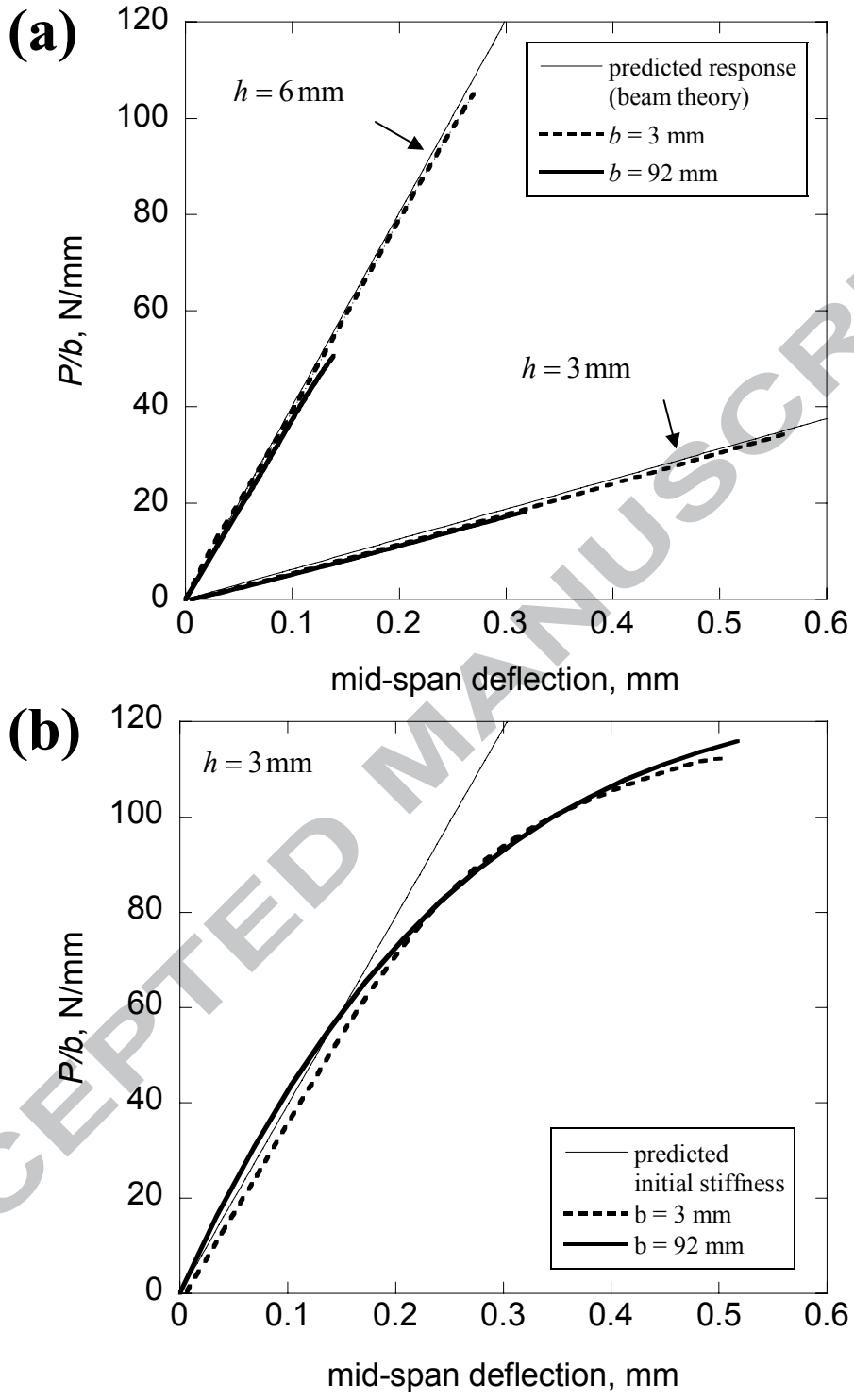

Fig. 9. (a) Measured and predicted normalized load versus mid-span deflection responses up to failure for composite beams of two different thicknesses. The prediction is obtained by beam theory and includes the effect of deflections due to shear. (b) Measured and predicted normalized load versus mid-span deflection responses for aluminium beams of the geometry indicated. Tests were interrupted at a deflection of 0.5 mm.

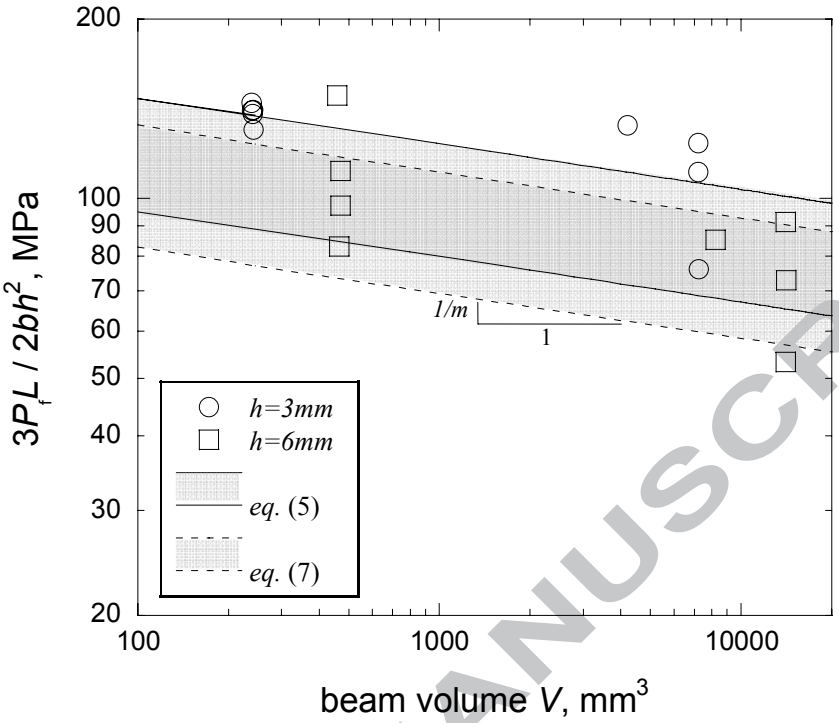

Fig. 10. Maximum tensile stress at failure versus specimen volume for the beam bending experiments. The failure stress decreases with increasing beam volume; the figure includes a prediction from eqns. (5) and (7).